JOURNAL OF GEOPHYSICAL RESEARCH, VOL. 112, B05204, doi:10.1029/2006JB004558, 2007

A new strategy for discrete element numerical models: 2. Sandbox applications

David Lundbek Egholm,[1] Mike Sandiford,[2] Ole Rønø Clausen,[1] and Søren Bom Nielsen[1]

Received 9 June 2006; revised 14 November 2006; accepted 8 December 2006; published 5 May 2007.

[1] Here we present a series of numerical experiments using a new formulation of the discrete element method (DEM) that improves performance in modeling faults and shear zones. In the new method, named the stress-based discrete element method (SDEM), which is introduced in the companion paper by Egholm, stress tensors are stored at each circular particle. Further, SDEM includes rotational resistivity of particles and elastoplastic constitutive rules for governing particle deformation. When combining these new features, the SDEM is capable of reproducing the friction properties of rocks and soils, without the need for the ad hoc calibration routines normally associated with DEM. In contrast to the conventional DEM, the friction properties of a SDEM particle system are in agreement with the Mohr-Coulomb constitutive model with friction angles specified on a particle level. "Benchmark" sandbox models show that unlike most commonly used numerical methods, SDEM faults and shear zones develop at angles in agreement with general observations from structural geology and analogue modeling studies.

Citation: Egholm, D. L., M. Sandiford, O. R. Clausen, and S. B. Nielsen (2007), A new strategy for discrete element numerical models: 2. Sandbox applications, *J. Geophys. Res.*, *112*, B05204, doi:10.1029/2006JB004558.

1. Introduction

[2] Discrete computational methods like the discrete element method (DEM) [*Cundall and Strack*, 1979; *Donze et al.*, 1994] are useful for gaining insight into the granular processes controlling the deformation style of rocks and soils. Using computers, experiments may be repeated with varying input parameters and the results of their variation are readily accessed and visualized by the modeler. Reliable modeling of geomechanic processes enables the structural interpreter to constrain the dynamic interpretation of the structures observed. Importantly, with respect to mapping of structures in the hydrocarbon industry mainly using two- and three-dimensional seismic data, modeling may help in predicting the deformation in areas with poor data quality (e.g., in a gas filled reservoir) or in predicting the orientation and size of structures of a size below the resolution of the seismic data used.

[3] Compared with the continuum methods used in geomechanical modeling, the discrete methods hold significant advantages when it comes to modeling granular flows. For example, dilatation effects important for initiating shearing instabilities are hard to capture with a continuum formulation but are readily embedded in the discrete methods, as these are based on particle assemblies including natural porosity measures. Further, as the discrete methods are meshless, they allow for very large deformations and complex geometries.

[4] However, the use of DEM has until now been limited by its inherent difficulties in reproducing the correct macroscopic friction properties of rocks and soil. In essence, DEM is based on micromechanical interactions between particles at contact points, and hence the method operates with a microscopic parameterization. Yet, in structural geology and other earth science disciplines, macroscopic constitutive relations (like the Mohr-Coulomb failure criterion) are often the most relevant for understanding a particular mechanical scenario. In these situations DEM performs relatively poorly as the relations between the model's microscopic and macroscopic properties are not straightforward and have to be calibrated through a somewhat ad hoc procedure of experimentation. The purpose of the new stress-based discrete element method (SDEM) as presented here, is to allow for more accurate simulations of the mechanical behavior of rocks and soil, or more generally, what is known as cohesive-frictional materials. Unlike standard discrete methods SDEM works with a macroscopic parameterization with macroscopic constitutive relations implemented at particle level, while still preserving the many advantages related to the discrete nature of DEM at the expense of a modest computational overhead.

[5] The fundamental ideas of SDEM, including the theory and equations for SDEM contact dynamics as well as quantitative tests validating the method, have been presented in the companion paper by *Egholm* [2007]. Here, in this second part of the SDEM presentation, we demonstrate applications based on proposed "benchmark" sandbox models. Although the numerical techniques are not restricted to the limited set of configurations and boundary

[1]Department of Earth Sciences, University of Aarhus, Aarhus, Denmark.
[2]School of Earth Sciences, Melbourne University, Parkville, Victoria, Australia.

0148-0227/07/2006JB004558$09.00

conditions normally associated with sandbox models, the adoption of a benchmark modeling approach provides a useful framework for evaluating the performance of new methods. The use of analogue sandbox models has a long history, and the experience derived from such model experiments form an excellent basis for testing how well SDEM reproduces structures that are relatively well understood.

[6] This approach to comparing numerical and analogue models has recently been systematized by *Buiter et al.* [2006], who has suggested specific benchmark experiments for both analogue and numerical models. The benchmarks include extension and shortening boundary conditions, involving the formation of both normal and thrust faults, respectively. In section 3 we evaluate how SDEM performs when adopting the benchmark model setups proposed by *Buiter et al.* [2006]. In addition, we model extensional "fault propagation folding" associated with deformation of relatively "soft" sediments overlying rigid basement cut by an active normal fault. This phenomenon has received considerable attention, and has been previously modeled with both analogue and numerical methods [*Dahl*, 1987; *Withjack et al.*, 1990], including DEM [*Finch et al.*, 2004]. In the previous discrete analysis, models of fault propagation folding have employed a purely cohesive proxy for sediment strength. Using the new SDEM modeling technique we are able to emphasize the importance of including appropriate frictional effects, resulting in much greater conformity with analogue experiments.

[7] For completeness, the basic ideas behind the new method are briefly presented first (for a richer and general treatment of the SDEM theory, we refer to *Egholm* [2007]).

2. Basis of SDEM

[8] In keeping with its DEM ancestry the stress-based discrete element method (SDEM) treats rock mass as an assemblage of circular discs or spheres, interacting in pairs at contact points. The circular elements, referred to as particles, are assumed elastic.

[9] As a new feature in discrete modeling SDEM introduces at each particle center a strain rate tensor recording the elastic deformation rate. Accumulated particle deformation is generally very small as contact sliding, and to some degree particle rolling, are the predominant deformation mechanisms. For this reason, the circular shape of each particle is retained through a model simulation. Importantly, however, the strain rate tensor is used for calculating the particle stress state which then determines the contact forces acting between particles.

[10] In SDEM each particle is considered a solid with its own mass, moment of inertia, and elastic as well as friction properties. On the basis of a computational scheme for estimating accelerations at each discrete time step, the particle motions are explicitly time integrated using Newtonian physics. In this paper, we restrict the formulation to cases where two-dimensional plane strain conditions prevail.

[11] The total force exerted on each particle is found by summing the force of gravity, and the forces acting at each of the particle's contact points. For particle a this is

$$F_a^i(t) = \sum\nolimits_b f_{ab}^i(t) + m_a g^i \tag{1}$$

where the first term on the right hand side is a sum of all particle a contact forces. Subscripts a and b are particle labels. g^i is the acceleration of gravity.

[12] The contact forces, f_{ab}^i, are found from stress tensors carried by the particles. If particles a and b are in contact, the force at their contact point (or more correctly their contact surface) is

$$f_{ab}^i = -\left(R_a \sigma_a^{ij} + R_b \sigma_b^{ij}\right) n_{ab}^j \tag{2}$$

where R_a, R_b, σ_a^{ij} and σ_b^{ij} are, respectively, the radii and stress tensors of particle a and b. Further, n_{ab}^i is the unit vector pointing from the center of particle a to the center of particle b. In equation (2) Einstein's summation convention of repeated indices is adopted for the superscripts.

[13] Stress tensors are updated using the strain rate measure and a simplistic elastoplastic constitutive rule. This way, Mohr-Coulomb conditions can be imposed directly at particle level, causing shear stress and tangential contact forces never to exceed the limits defined by the friction angle. Additionally, and in contrast to existing DEM formulations, this technique allows for stress relaxation at a subparticle scale. This is important, since the discrete numerical models can only handle a limited (10^5–10^7) number of particles; a number which is often several orders of magnitude lower than the true number of grains embodied in the piece of rock or soil being modeled. Hence the numerical models do not consider every grain of the granular matter. Rather, the particles themselves represent a piece of particulate matter with the possibility of internal sliding. As shown by *Egholm* [2007], this stress updating procedure of SDEM results in more realistic macroscopic stress fields as compared to existing conventional discrete element methods.

[14] The constitutive parameters are specified at particle level and include Young's modulus, E, Poisson's ratio, ν, the angle of internal friction, ϕ, and cohesion, C. Particle rolling is reduced by rolling resistivity, introducing at each particle an angle of rolling resistivity, ψ_r. This angle defines the slope, at which the particle will start rolling under the influence of gravity when placed on a base with similar frictional properties. Generally, if $\psi_r > \phi$ contact sliding is the dominant deformation mechanism. In contrast, if $\psi_r < \phi$ particle rolling is widespread. In all models presented here $\psi = 40° > \phi$.

[15] Time steps are limited by

$$\Delta t < \min\left(\sqrt{\frac{\rho R^2}{K}}\right) \tag{3}$$

where R is particle radius, ρ is density and K is bulk modulus. Boundary conditions are typically enforced by moving rigid walls at speeds well below the speed of sound ($\sqrt{K/\rho}$) ensuring the particles moves under quasi-static stress conditions. All SDEM models presented in this paper share the following invariable parameters: $E = 10^{10}$ Pa, $\nu = 0.25$ and $\rho = 2700$ kg/m^3. Average porosity of the particle assemblages used is 15% yielding an average assemblage density of $\bar{\rho} = 2300$ kg/m^3. Cohesion is lost when the accumulated particle strain exceeds $\varepsilon_c = 0.1$. The latter effect softens material when deforming, and is in part responsible for localization of strain in shear zones. The

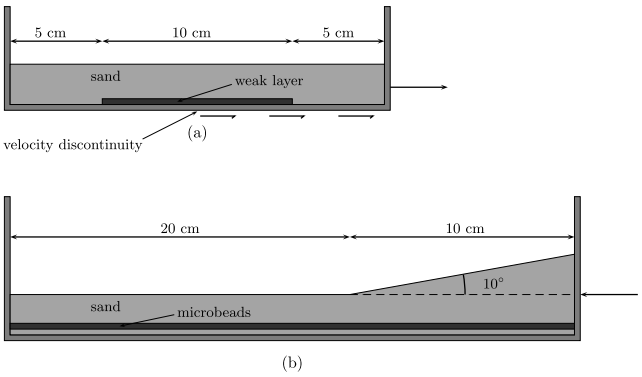

Figure 1. Model configurations for (a) the extension and (b) the shortening benchmark experiments.

other effect contributing to strain softening relates to dilatation (increasing porosity and decreasing pressure) of initiating shear zones. Shear zone dilatation, which is addressed further in section 5, is an implicit part of the discrete kinematics, as pore space generally grows when densely packed particles are forced to slide past each other. Other softening effects possible to incorporate in SDEM include strain-induced changes to the friction or rotation related properties (the angle of internal friction and the angle of rolling resistivity), in turn reflecting changes to particle shape and roughness triggered by shear deformation. However, these latter softening effects are not considered here.

3. Sandbox Benchmarks

[16] Numerical sandbox models generally suffer from a low degree of comparability, due to the diversity of techniques used for approximating the mechanics of granular materials and for implementing boundary conditions. Analogue sandbox models are troubled by similar issues as model apparatus, modeling materials and monitoring strategies vary significantly among laboratories. However, in an attempt to assess the reliability of sandbox models, two recent studies have suggested benchmark experiments for testing the reproducibility of analogue laboratories [*Schreurs et al.*, 2006] and numerical codes [*Buiter et al.*, 2006], respectively. In these studies, a shortening and an extensional model configuration reflecting setups commonly used in studying upper crustal tectonic processes are outlined, and results from 10 analogue laboratories and eight different numerical codes are compared. Of the numerical codes one is based on the conventional discrete element method (PFC^{2D} implementation) [*Itasca Consulting Group, Inc.*, 1999; *Cundall and Strack*, 1979], the others are based on finite element or finite difference implementations of elastoplastic, viscoplastic or viscoelastoplastic continuum formulations.

[17] The model experiments are not benchmarks in the strict sense, as this would require identical model setups, material properties and boundary conditions, which unfortunately are provisions the diversity in modeling techniques do not allow for. However, the benchmarks suggested by *Schreurs et al.* [2006] and *Buiter et al.* [2006] are useful in making qualitative and semiquantitative comparisons.

[18] Here, we use the *Schreurs et al.* [2006] and *Buiter et al.* [2006] benchmark studies as a basis for testing the performance of SDEM against both analogue and numerical sandbox modeling methods. The overall deformation style of the SDEM models provide a qualitatively test of SDEM while comparisons of shear zone orientations provides a quantitative test. The two benchmark model configurations used to evaluate SDEM are shown in Figure 1.

3.1. Brittle Extension Benchmark Experiment

[19] The extension benchmark experiment involves a 3.5 cm thick and 20 cm long sand layer of $\phi = 36°$ and $C = 10$ Pa. Embedded in the sand layer, near the model base, is a weaker layer of thickness 0.5 cm and length 10 cm (see Figure 1a). This layer is modeled by a viscous slap of silicone in the analogue models and by a linear viscous layer of viscosity 5×10^4 Pa s in the numerical models evaluated by *Buiter et al.* [2006]. In the SDEM model used here, the low strength layer is simply modeled by a low friction cohesive layer ($\phi = 1°$ and $C = 10$ Pa). In SDEM, a viscous constitutive relation could be implemented at particle level. However, this is beyond the scope of the theory presented and tested by *Egholm* [2007].

[20] The right vertical wall and the right half of the model base is moved at constant velocity $v = 0.01$ m/s, which is more than five orders of magnitude lower than the speed at which the elastic energy propagates (the speed of sound). In the comparable analogue models [*Schreurs et al.*, 2006] the friction conditions of the walls and model base are poorly constrained. For this reason, we have chosen for the SDEM model the simplest conditions possible, using frictionless vertical walls and a model base with $\phi = 36°$. It is noted, however, that the results of the extension experiment is rather independent of sidewall and base friction. At the midpoint of the model base a velocity discontinuity exists where new model base is continuously formed and being attached to the left static part. Hence, as the length of the right model base is kept constant and the left part is growing as the right part moves, the velocity discontinuity migrates to the right also at velocity v.

[21] The evolution of the SDEM model including 110,000 particles of radii $R \in [0.05; 0.20]$ mm is shown in Figure 2 as deforming layers (Figure 2a) and as strain rate contours (Figure 2b). A small graben defined by a set of steep (>60°) conjugate normal faults initiate in the model center over the basal velocity discontinuity. As the sand in the graben subsides new faults initiate to the right and left widening the deformation zone. Pressure gradients resulting from local thinning of the sand layer drive flow in the underlying weaker material toward the model center propagating further faults in the sand above. All faults migrate to the right with the velocity discontinuity, but at a reduced speed keeping the initial graben nearly centered in the model thereby resulting in a rather symmetric stretching style.

[22] The resulting complex fault pattern (displacement 5 cm shown in Figure 3) includes symmetric graben structures, half grabens, synthetic and antithetic fault systems, "bookshelf" faults and conjugate fault sets. The strain rate contours underlines how deformation is focused in the weak basal layer and in the shear zones. Initially, strain rates are high in the model center. At later stages, faults near the outer edges of the weak layer are the most active, while deformation continues in the inner faults at a reduced rate.

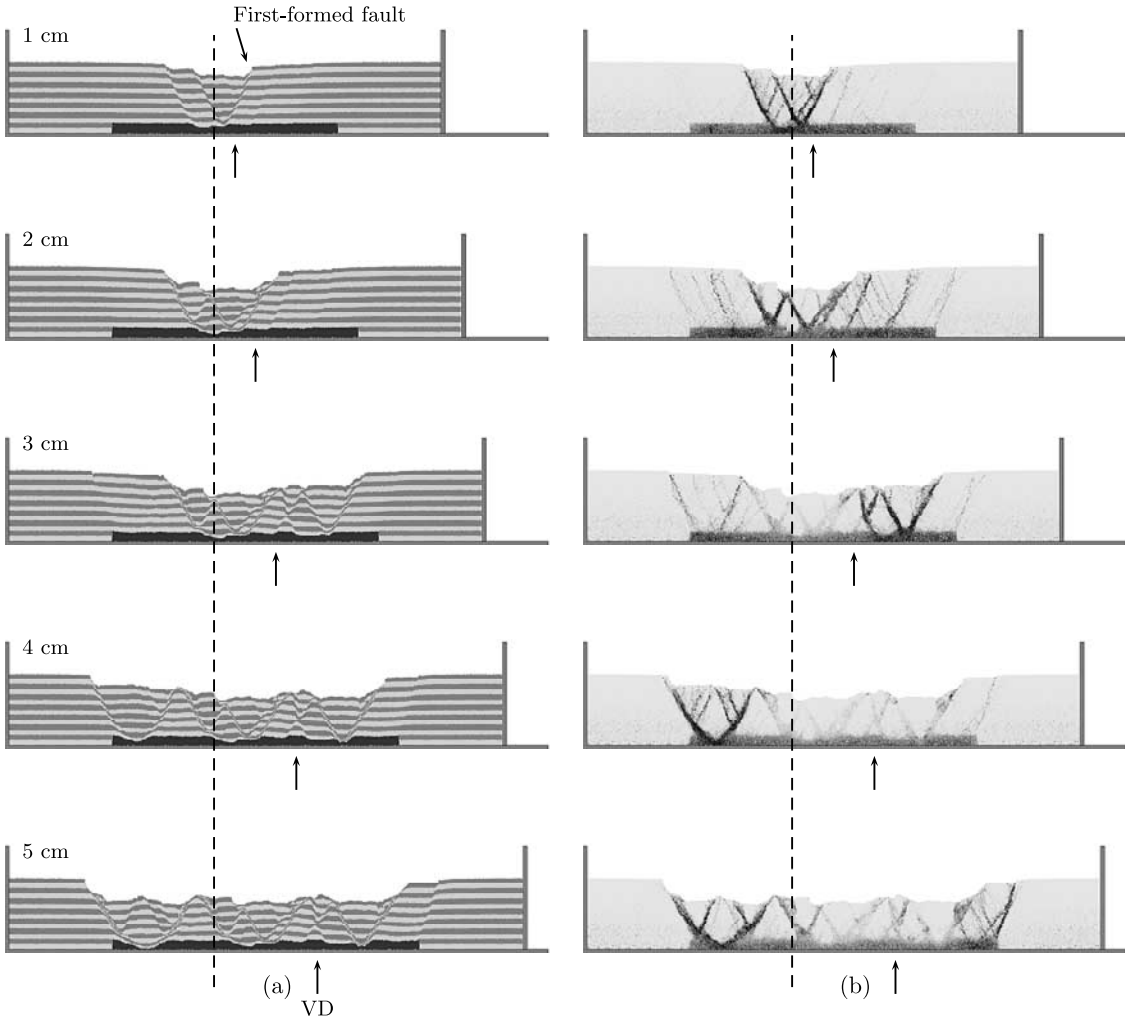

Figure 2. Results of the extension SDEM benchmark experiment. A time series of five snapshots presents (a) the deforming layers (sand layering is just coloring) and (b) strain rate contours. Vertical dashed lines represent the initial model center and vertical arrows indicate the position of the basal velocity discontinuity.

With increasing deformation, the locus of maximum strain rate oscillates from side-to-side across the deforming domain.

[23] When compared with analogue model results [*Schreurs et al.*, 2006], the SDEM deformation patterns agree well in a qualitative sense. Quantitatively, when measuring shear zone orientations, the SDEM model results fall closer to the analogue results reported by *Schreurs et al.* [2006], than to the numerical results presented by *Buiter et al.* [2006].

[24] In the extension experiment all analogue models show initiation of faulting in the model center, and propagation of faults toward the model sides with deformation. However, the number of faults created vary significantly among the analogue models, with some models forming only few rotating sand blocks (Florence and Piscataway experiments) and others predicting a highly dissected deforming sand layer (IFP Rueil-Malmaison experiment). The analogue model laboratories used different types of

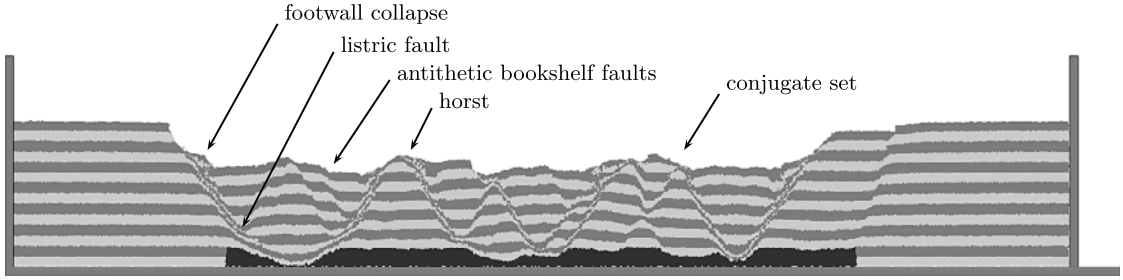

Figure 3. Enlarged view of the deformed layers at displacement of 5 cm.

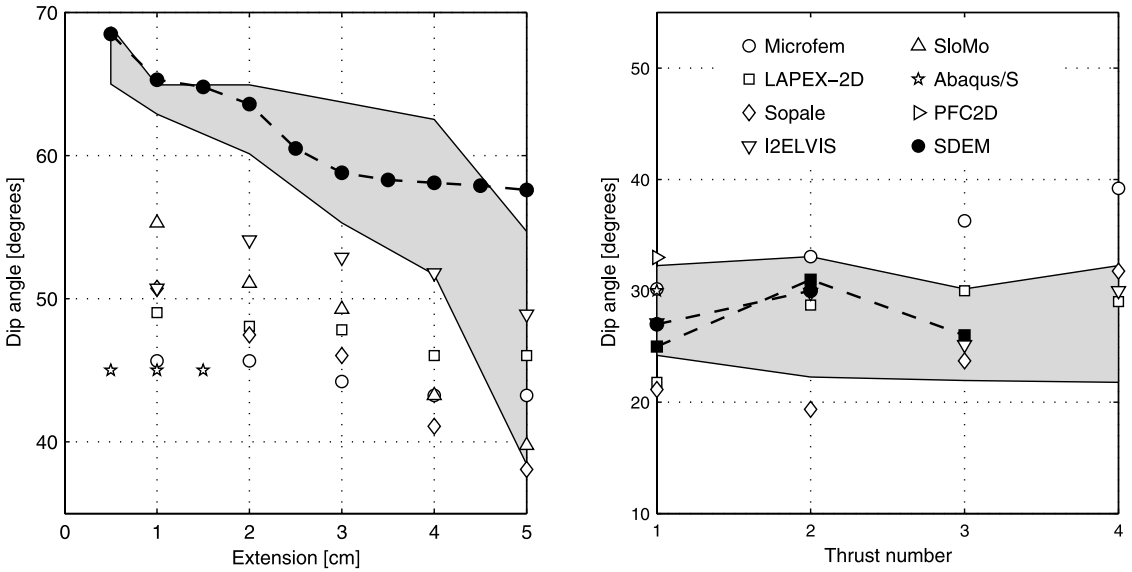

Figure 4. Shear zone orientations (dip) for (left) the extension and (right) the shortening benchmark experiments. For the extension experiment the dip of the first-formed normal fault is shown with increasing extension. For the shortening experiment, thrust orientations was measured at the time of their formation. The gray areas represent the results of the analogue experiments as reported by *Schreurs et al.* [2006]. Markers represent results of the numerical experiments as reported by *Buiter et al.* [2006]. Black dots and squares connected by a dashed line are the SDEM results (black squares represent the second shortening experiment presented in Figure 5b).

sand of varying ϕ and C (the Piscataway experiment actually used clay instead of sand). The faulting frequency of the SDEM extension model falls within the range predicted by the analogue experiments. For most of the analogue models the stretching style is rather symmetric with a tendency of the velocity discontinuity to migrate right faster then the first-formed graben structure (as shown in Figure 2b). However, in the late stage of the analogue models a clear asymmetry is visible, with the deformation locus being shifted to the right. The same tendency is not so clear in the SDEM model. This discrepancy is explained by the different strength proxies used for the weak layer, as the asymmetric behavior depends on the strength of the weak material, with higher strength facilitating a more asymmetric deformation style.

[25] The numerical extension experiments presented by *Buiter et al.* [2006] also confirm the general behavior of the SDEM model. Yet, there are marked differences in fault orientations predicted by the various models. We have measured quantitatively the fault orientations in the SDEM benchmark experiments and compare these with equivalent measures from the analogue and numerical experiments reported by *Schreurs et al.* [2006] and *Buiter et al.* [2006]. All results are shown in Figure 4 for both the extension (Figure 4, left) and the shortening (Figure 4, right) experiments.

[26] In the extension experiment the dip angle of the first-formed ''right-dipping'' normal fault (see Figure 2) was measured with increasing extension. The dip angles generally decrease with extension as the fault plane rotates (Figure 4, left). As evident, there is a consistent and marked difference in the initial dip angles as predicted by the analogue and numerical experiments tested by *Buiter et al.* [2006]. The analogue models show initial dip angles ($\sim$65°) significantly higher than the numerical models (45°–55°). The latter models are based on continuum viscoplastic or viscoelastoplastic formulations combined with incompressibility constraints causing shear zones to be nondilatant. For such model assumptions shear zones are expected to be oriented at angles between 45° (Roscoe angle) and 45 + ϕ/2 (Coulomb angle) [*Vermeer*, 1990]. SDEM on the other hand predicts an initial fault dip in agreement with the analogue model experiments. The fault dip starts at 67° and drops with extension to $\sim$57°, where the curve flattens as forming new faults at this stage requires less work than to further rotate the existing low angle normal faults. The initial fault planes are marginally curvilinear with higher dip near the model top. This general behavior signals, that near the model top where pressures are low cohesion is the dominant strength component, resulting in near vertical tensile cracks forming. The upward steepening of the initial fault plane is responsible for the slightly too high dip measures (63° is expected from Mohr-Coulomb theory and 67° is measured as the average initial dip of the first forming fault (see Figure 4)).

3.2. Shortening Benchmark Experiment

[27] The shortening benchmark experiment is outlined in Figure 1b. It includes a preexisting thrust wedge of length 10 cm and surface slope 10°. The total initial length of the sandbox is 30 cm. The model consists of a 3.5 cm thick sand (ϕ = 36° and C = 10 Pa) layer except for a 0.5 cm thick weaker layer embedded near the base of the model. The weak layer is modeled as ''microbeads'' with ϕ = 20° and C = 10 Pa. The friction angle of vertical walls is 20°, while the base friction angle is ϕ_{base} = 20° in one experiment and ϕ_{base} = 36° in another. Shortening is achieved by moving the right vertical wall to the left at speed 0.01 m/s with the

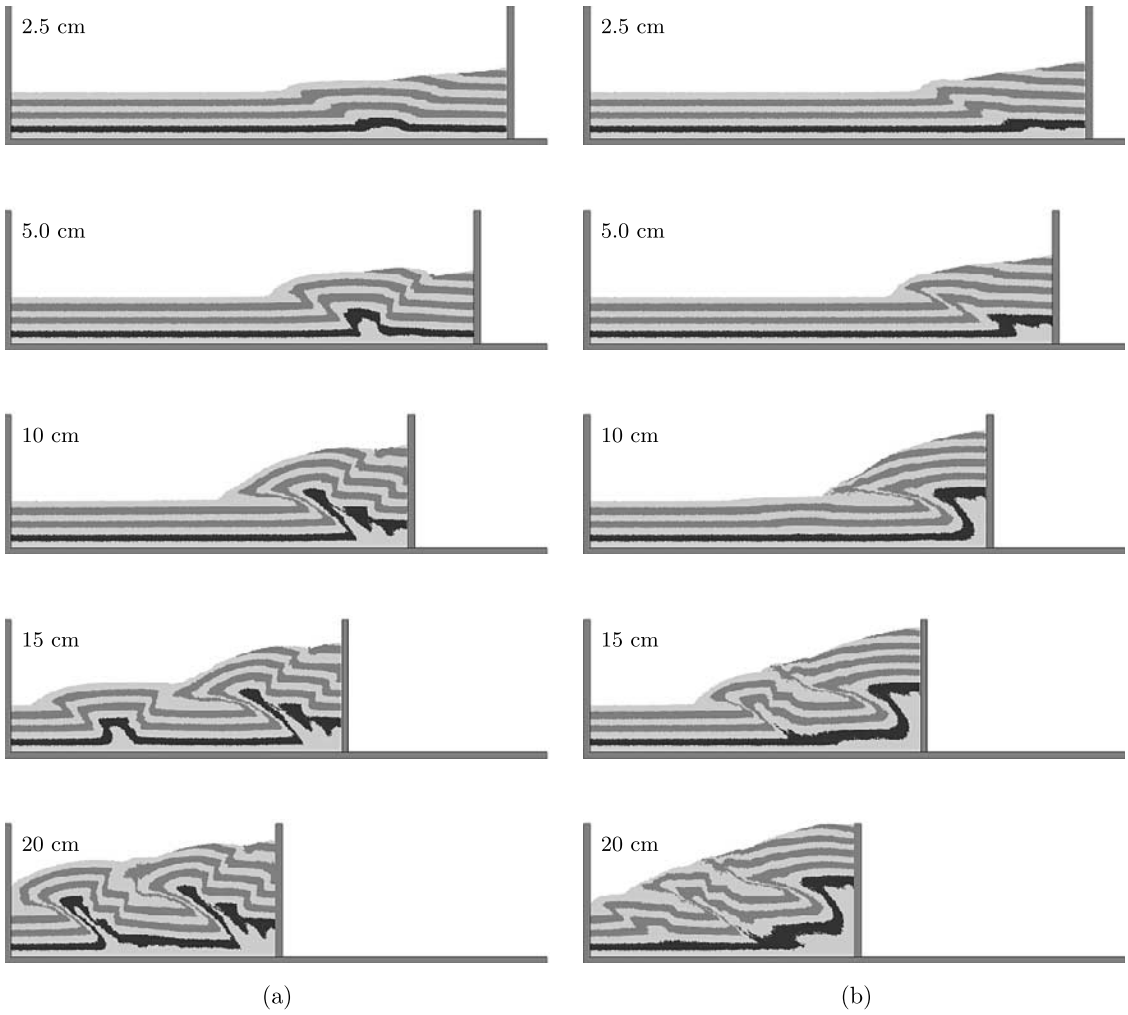

Figure 5. Two SDEM benchmark shortening experiments. For each experiment a time series of five snapshots is shown. The two models differ only in the basal friction. Experiments (a) $\phi_{base} = 20°$ and (b) $\phi_{base} = 36°$. The black layer represents weak microbeads, while gray layers all represent sand of uniform parameterization.

base and left vertical wall fixed. This model setup reflects a classic experiment applied frequently by modelers (both analogue [e.g., *Davis et al.*, 1983; *Colletta et al.*, 1991; *Storti and McClay*, 1995] and numerical [e.g., *Strayer et al.*, 2001; *Burbridge and Braun*, 2002]) to study the dynamics of propagating thrust wedges as found in orogenic belts and at convergent margins. In this particular setup the low strength microbeads layer or the model base can act as agents for propagating thrusts in front of the evolving convergent wedge.

[28] Figure 5 presents the two SDEM models with different base friction angles ($\phi_{base} = 20°$ for Figure 5a and $\phi_{base} = 36°$ for Figure 5b) and both including 60,000 particles with $R \in [0.1; 0.4]$ mm.

[29] The two models generally display the same overall behavior. In both, thrust faults develop in the right part of the model and propagate to the left with increasing shortening. The thrusts propagate to the left as the height of an active thrust wedge grows, reflecting the fact that at some critical height it requires less work to activate a new thrust wedge, than to keep building the height of the existing thrust wedge. For both models the maximum surface slopes measured are just less than 30°. There are, however, also significant differences caused by the varying friction angle of the model base.

[30] In the model of Figure 5a the first thrust and an associated back thrust develop from a point below the tip of the initial preexisting thrust wedge. As the thrust wedge grows (displacement 5 and 10 cm) multiple back thrust are formed traversing the preexisting wedge. At a displacement of 15 cm a new thrust wedge is generated in front of the existing. The new thrust wedge is positioned such that the tip of its associated back thrust align with the tip of the old thrust. With further displacement more back thrusts develop in the new active wedge, and the comparability of the old and new wedge geometries increases. In propagating the thrusts, the model base acts as the main detachment surface.

[31] In the second shortening experiment the base friction is higher, and hence the model setup is more resistant to thrust fault propagation. The first thrust fault develops under the preexisting thrust wedge, and as such, the initial model behavior is to further build the preexisting wedge. At 10 cm

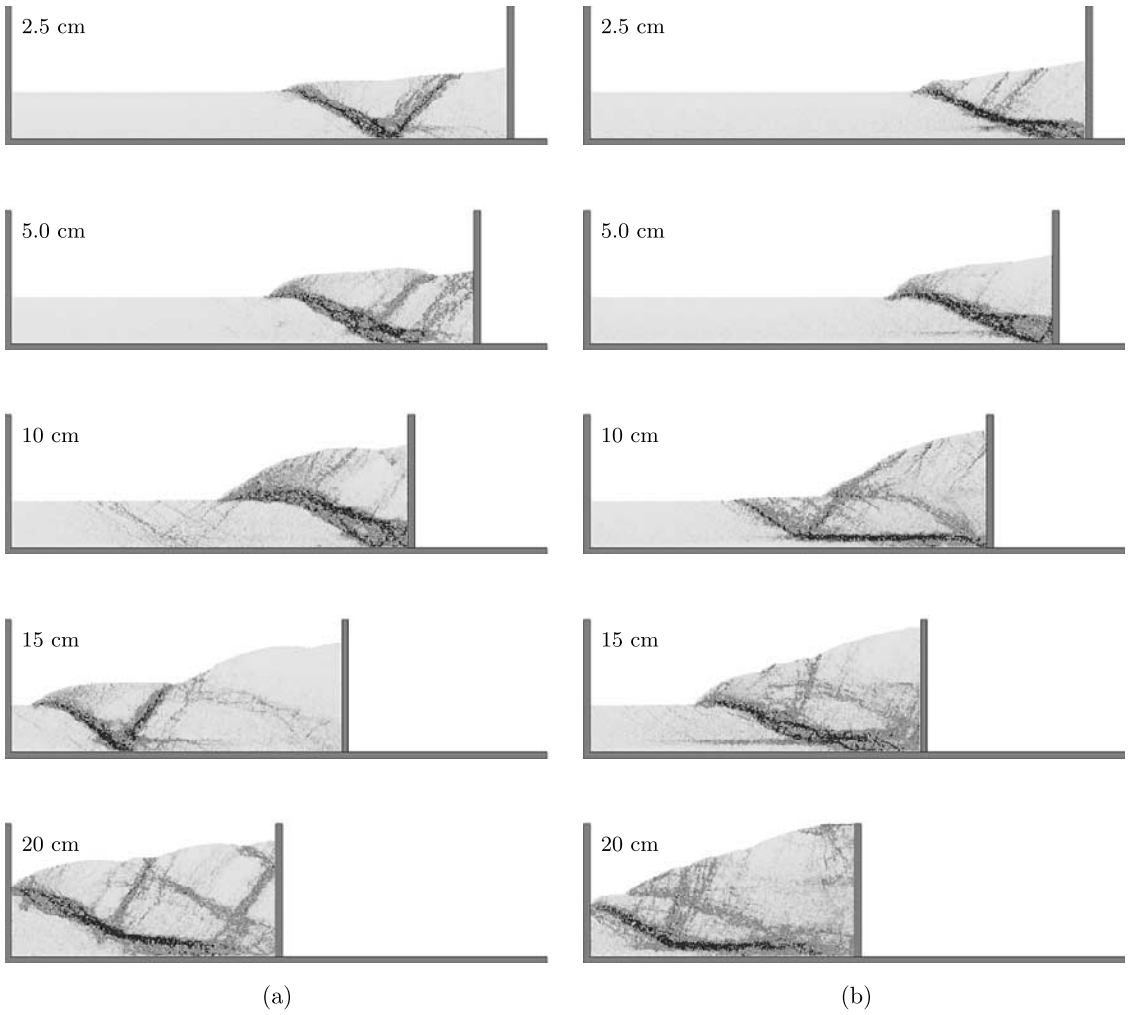

Figure 6. Strain rate contours matching the deformed configurations of Figure 5. In Figure 6b, note the importance of the weak microbeads in propagating strain rates.

displacement a new thrust wedge is initiated in front and partly below the existing. The weak layer of microbeads is the agent for thrust propagation as it now delivers the main detachment surface (see Figure 6b, third panel, where strain rates are shown). At 20 cm displacement a third thrust wedge is formed again partly underlying the previous.

[32] In the shortening experiment the analogue models reported by *Schreurs et al.* [2006] show some degree of variation due to the variability in material properties used. Still, with deformation all show the propagation of thrust away from the moving wall. In some of the analogue shortening experiments the thrusts propagate easier than in other analogue experiments where the preexisting thrust wedge is built high before propagation initiates. To some degree, these differences are much like what differentiate the two SDEM models shown in Figure 5, indicating that small variations in basal friction can partly explain the diversity of analogue model predictions. The continuum-based numerical experiments presented by *Buiter et al.* [2006] also show the same general trend with a high degree of mutual consistency. Yet, a few distinct differences exist between the continuum numerical models on one hand and the SDEM and analogue models on the other. The continuum models quite consistently predict the first thrust to develop from the right lower corner of the model, whereas in the analogue and in the SDEM models the thrust initiates from a basal point to the left of the right lower corner. This discrepancy probably relates to the difficulty of including in continuum models discontinuous velocity boundary conditions [*Buiter et al.*, 2006]. In addition, in the analogue models and in the first SDEM shortening experiment (Figure 5a) back thrusts are a distinct feature developing after only a few centimeters of displacement. In the continuum models back thrusts are much less evident. As *Buiter et al.* [2006] point out, this absence of back thrusts may link to the just mentioned preference of the continuum models for the first thrust to initiate at the basal right corner. One discrete DEM shortening model (PFC^{2D} implementation) is included in the models presented by *Buiter et al.* [2006]. This discrete model also shows back trusts developing, confirming that back trusts should develop naturally in this model scenario.

[33] For the shortening experiment the dip angle of the thrust faults was measured at the time of their formation. In contrast to the marked differences seen in the extension experiment, all dip angles for the shortening experiment fall

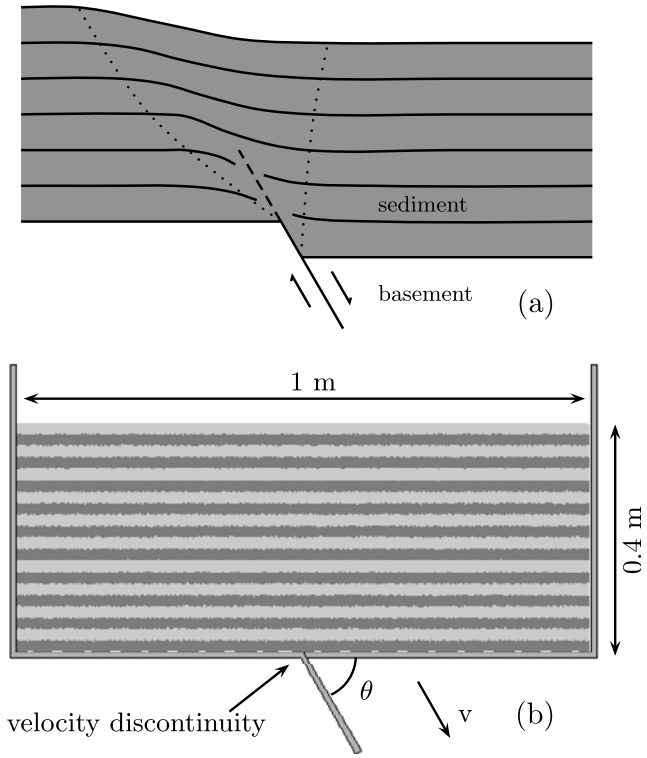

Figure 7. Sketch of an extensional fault propagation folding experiment with a 60° dipping normal fault. (a) General observations showing initial folding of the sediment strata and later basement fault propagation [after *Withjack et al.*, 1990]. (b) Setup and boundary conditions of the SDEM experiments.

around 30° as evident from Figure 4 (right), indicating a higher degree of consistency between analogue and numerical experiments including SDEM.

4. Fault Propagation Folding

[34] The benchmark experiments outlined in section 3 suggest that SDEM holds many prospects for simulating natural geological materials with friction properties. In this section we use the SDEM method for exploring just one such natural geological scenario known as fault propagation folding. Fault propagation folding occurs where a sequence of relatively soft sediment deforms under the influence of a blind underlying basement fault, and where a characteristic upward changeover from faulting to folding is observed in the sediment. Generally, the sediment is vertically offset along a monocline more or less in upward extension of the basement fault trace (see Figure 7a). Fault propagating folding is often observed in sedimentary basins and has attracted much attention due to, among other reasons, its importance for understanding seismic hazards, hydrocarbon migration and trap development, and naturally, for the general understanding of basin dynamics.

[35] The mechanics of fault propagation folding have been studied in both analogue [*Withjack et al.*, 1990] and numerical experiments [*Patton and Fletcher*, 1995; *Finch et al.*, 2003, 2004]. In the numerical studies of *Finch et al.* [2003] (contractional) and *Finch et al.* [2004] (extensional) a discrete element approach was chosen, which allow the sediment folds and faults to develop in a self-consistent unforced manner. The friction properties of the sediment modeled were however ignored, and radial elastic breakable bonds between circular particles were used as the only proxy for sediment strength. On the basis of their modeling results, *Finch et al.* [2004] concluded that the dip of the basement fault has a strong influence on both hanging wall and footwall sediment kinematics. Particularly, the width of the deformation zone and the dip of the propagating overburden faults were observed to be strongly influenced by the basement fault dip, with the sediment faults propagating at approximately the same angle as the basement fault. These DEM studies of *Finch et al.* [2004] provide a useful framework for assessing whether SDEM provides additional insights.

[36] Therefore we reproduce the experiments of *Finch et al.* [2004] and describe the differences obtained with the more accurate treatment of sediment frictional strength SDEM offers. We will concentrate on the extensional setting as outlined in Figure 7, where 62,000 particles of $\phi = 30°$ and $C = 10$ Pa represent a sand layer of width 1 m and height 0.4 m. The particle radii range between 0.05 and 0.5 mm. A discrete basement normal fault divides the model base into a moving right part (hanging wall) and a left part at rest (footwall). The right model part is moved downward in the slip direction of the normal fault at speed $v = 0.01$ m/s. Figures 8a–8c show three models with basement fault dip of $\theta = 30°$, 45°, and 60°, respectively. Figures 8 (left) and 8 (right) show the models at low and high basement fault slip, respectively.

[37] For low basement fault dip (Figure 8a) the horizontal component of the velocity discontinuity at the model base is relatively high, and as a result two faults (a synthetic and an antithetic) develop in the sand layer. Generally, the horizontal velocity discontinuity acts to stretch the model, and if no vertical velocity discontinuity was present, two conjugate normal faults would develop delimiting a small symmetric graben structure as in the extension benchmark model of section 3.1. However, in the case shown in Figure 8a the basement fault dip is 30°, and at large fault slip (Figure 8, right) a clear asymmetry is evident.

[38] As the basement fault dip increases (Figures 8b and 8c) the size of the horizontal velocity discontinuity decreases and the antithetic fault becomes less apparent. For $\theta = 60°$ the internal displacements of the hanging wall is accommodated only by a gentle syncline (hanging wall rollover).

[39] In all three models a synthetic fault propagates in the footwall to the left of the velocity discontinuity. The fault initially develops as an upward widening monocline. In the late stage (Figure 8, right) the monocline is breached near the base of the sand layer, as well as near the surface, where small-scale normal faults advance the gravitational collapse of the monocline limb.

[40] In contrast to the kinematics of the hanging wall, the footwall part of the models is relatively unaffected by the variation in basement fault dip. In particular, the dip of the synthetic fault is consistently 60°–65° independently of the basement fault dip. This is expected from Mohr-Coulomb theory, as the fault orientation ($\theta = 45° + \phi/2$) is linked to the internal friction properties of the sediment, which in turn do not vary between models.

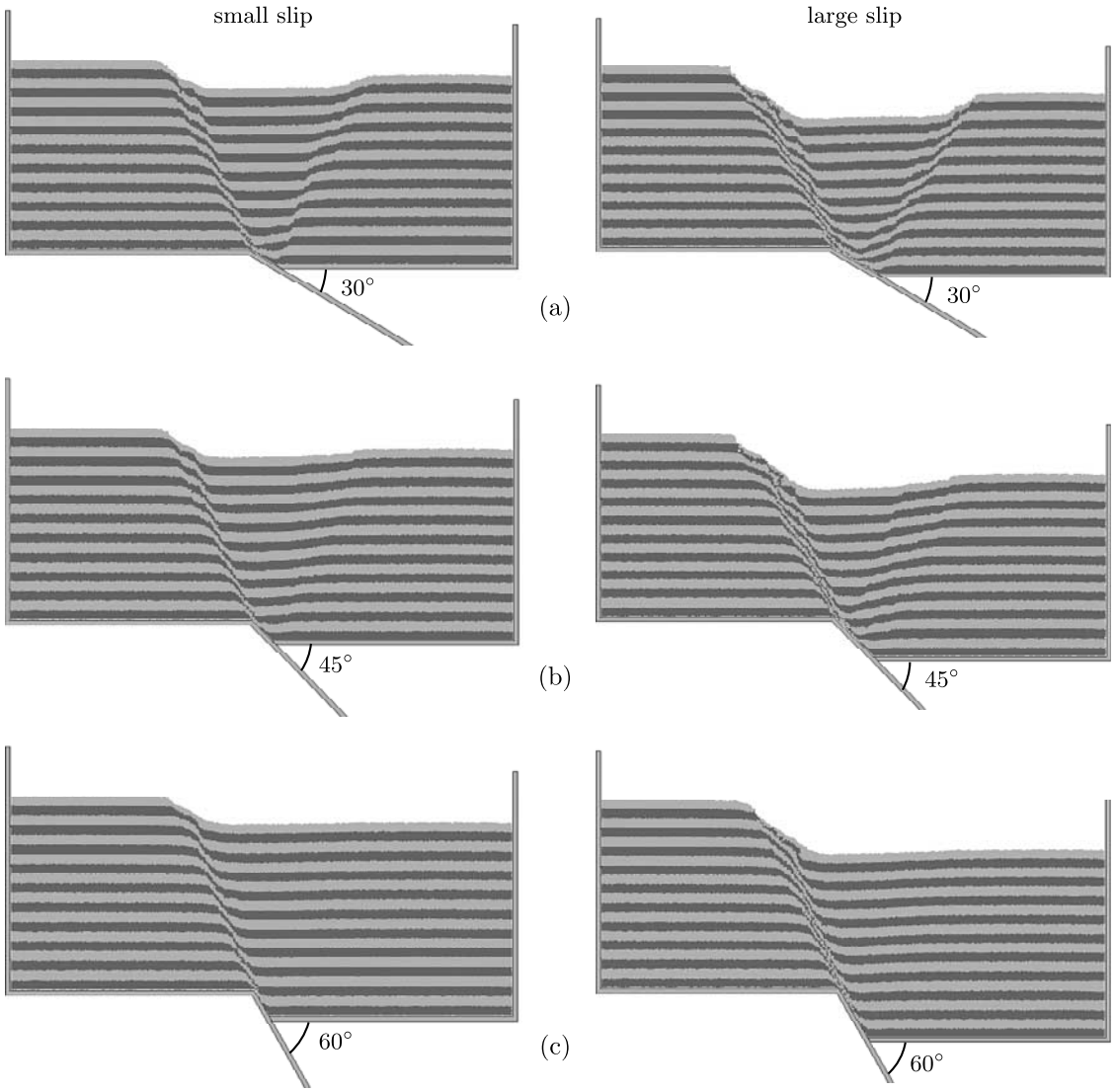

Figure 8. Fault propagation folding experiments with basement fault dip of (a) 30°, (b) 45°, and (c) 60°. The three experiments at (left) an early and (right) a later stage in the model evolution with basement fault slip of 6 and 12 cm, respectively.

[41] However, this behavior is contrary to the conclusions of *Finch et al.* [2004]. Using a frictionless version of DEM, *Finch et al.* [2004] modeled basement fault dips of 30°, 50°, and 70°. The resulting synthetic sediment fault were seen to propagate at angles of 40°, 50°, and 70°, respectively. From this, *Finch et al.* [2004] concluded that fault propagation through sediment depends heavily on the basement fault dip. Importantly, because *Finch et al.* [2004] used a purely cohesive model for sediment strength, they do not include a mechanism for determining fault dip in a frictional material. As a consequence, it is the boundary conditions of the model that dominate the faulting behavior. Using SDEM, we can see that internal properties of frictional materials are more likely to provide the dominant control on the faulting behavior.

[42] Figure 9 demonstrates the behavior of sand in analogue models under kinematic conditions as used in the SDEM models (Figure 8). Here, photos of analogue models with $\theta = 30°$, 45°, and 60° and using dry sand of $\phi \sim 30°$ and $C \sim 10$ Pa for representing the sediment overburden, are shown at stages comparable to Figure 8 (right). At a qualitative level the analogue and SDEM models are consistent, both generating steep synthetic faults with orientations independent of the basement fault dip. Of note also is the fact that the hanging wall behavior is similar in both analogue and SDEM experiments with antithetic faults developing for $\theta = 30°$ and none for $\theta = 60°$. In the latter case, both analogue and SDEM experiments show a gentle hanging wall rollover developing.

5. Discussion and Conclusions

[43] Dynamic computational models of faults and shear zones are confronted with many challenges. The rock mechanical behavior leading to formation of fault systems is highly nonlinear and involves large and localized shearing deformations, and in addition, the mechanical principals governing the physics of granular shearing are far from

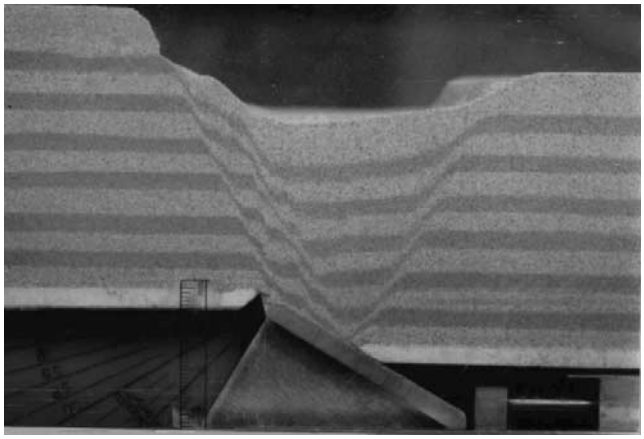

(a)

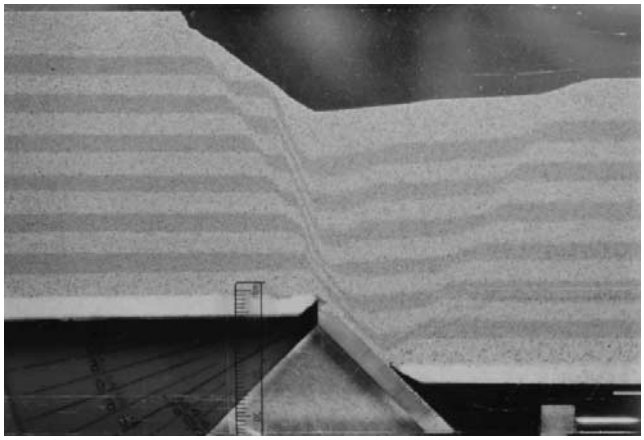

(b)

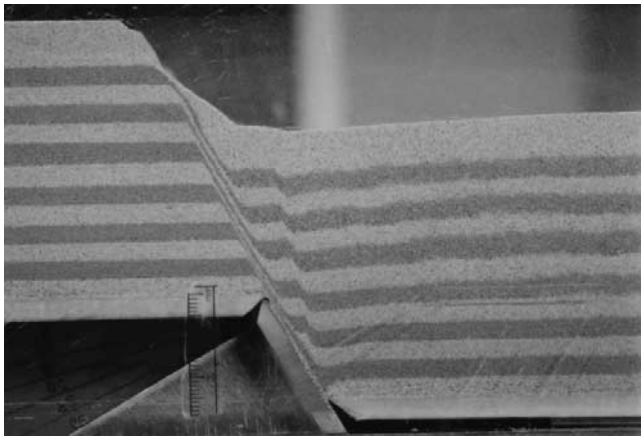

(c)

Figure 9. Photos of analogue fault propagation folding model experiments [after *Dahl*, 1987]. The analogue model setup resembles that of the SDEM experiments with basement fault dips of (a) 30°, (b) 45°, and (c) 60°.

being completely understood. Two basically different types of model strategies are often used when fault systems are being modeled computationally. One discrete strategy involves studying strain localizing processes on a microscale, explicitly modeling the dynamics of grain interactions. Research in this area often makes successful use of the discrete element method (DEM) in seeking to bridge the gap existing between our microphysical and macrophysical understanding of granular flows.

[44] Another strategy involves modeling fault systems on a macroscopic scale in seeking dynamic explanations for the kinematics of natural fault structures. In this case, models are most likely based on macroscopic constitutive rules using established bulk load displacement curves for the modeling material involved. The macroscopic elastic, viscous and/or plastic constitutive relations are often implemented using continuum-based formulations of the mechanical equilibrium equations or equivalent energy and mass conserving principles. The advantage of the continuum approach is that one can specify directly the material behavior using the macroscopic properties, which at the same time represent an appropriate basis for understanding the dynamic evolution of the fault systems on the macroscale. On the other hand, continuum models are most often mesh based, using finite element or finite difference schemes for solving the differential equations involved. A mesh greatly complicates modeling of strain localization, as the large deformation heavily distort the mesh making an initial optimized mesh geometry ineffective for continued use. One way of avoiding this problem involves using Eulerian [e.g., *Moresi et al.*, 2002; *Gerya and Yuen*, 2003] or ''arbitrary Lagrangian-Eulerian'' (ALE) [e.g., *Fullsack*, 1995; *Ellis et al.*, 2004] formulations in which material is more or less advected through the mesh, and the mesh can therefore be kept undistorted. Most of these methods were generally developed for simulating large-scale mantle and crustal deformation processes, not giving high priority to the precise evolution of individual fault systems, and their use has only lately been extended to include structural geology application on the ''sandbox scale.'' Several such continuum-based sandbox models were evaluated by *Buiter et al.* [2006] with generally good results. However, as shown by *Buiter et al.* [2006] and in Figure 4, this type of modeling approach seems to have difficulties in predicting realistic fault orientations, which in turn indicates that the dynamic conditions of the granular material being simulated are not accurately reproduced by the methods.

[45] Of known key importance for capturing the true dynamics of fault zone development is the treatment of material dilatation during shearing. Granular matter, as sand and shale, dilate when being sheared, as the void volume generally increases when grains are forced to slide past each other. This effect softens material inside shear zones and is in part accountable for the development of strain localizations in rocks and soils. The continuum methods evaluated by *Buiter et al.* [2006] applied incompressible plastic flow rules preventing dilatation, which in turn could be responsible for the models' poor performance in reproducing fault orientations realistically.

[46] For most of the continuum model methods evaluated by *Buiter et al.* [2006] dilatation can in fact be considered, as most of the continuum formulations make use of nonas-

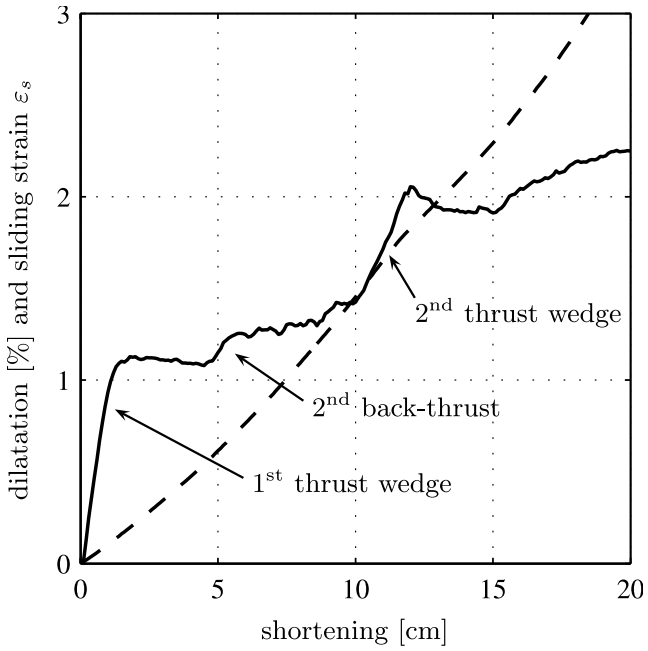

Figure 10. Dilatation (solid curve) and sliding strain (dashed curve) versus shortening for the first shortening experiment of Figure 5a. As particle radii are invariant, dilatation equals the relative growth of pore space volume. Three periods associated with shear zone formation and rapidly increasing dilatation are identified on the graph. For comparisons with associated model geometries, see Figure 5a.

sociated plasticity models [*Vermeer and De Borst*, 1984] for representing brittle failure. The nonassociated models introduces an angle of dilatation often operating as a proportionality factor between dilatation rate and plastic strain rate. However, proportionality between dilatation and strain is most likely not a valid assumption. Experimental observations indicate [*Vásárhelyi*, 1999] that dilatation rate and sliding strain are nonlinearly related, with dilatation rates being initially high during shear band formation, and tending to zero once sliding is attained within the shear band. For continuum methods to reproduce such nonlinear dilatation effects more sophisticated plasticity models are required, as the one lately developed by *Crook et al.* [2006a]. This particular constitutive model is based on critical state concepts and includes a stress state-dependent dilatation angle. When implemented in a fully Lagrangian finite element framework, the constitutive model is able to reproduce correctly the shear orientations of real faults [*Crook et al.*, 2006a, 2006b]. For handling the large amount of sliding deformation, the Lagrangian finite element approach does depend, however, on efficient remeshing techniques.

[47] Discrete modeling methods including SDEM, on the other hand, have an implicit way of representing granular dilatation, as the particle kinematics automatically leads to dilatation when shear zones develop. Figure 10 shows dilatation and sliding strain as a function of shortening for the first shortening experiment of section 3.2 (Figure 5a). Model dilatation (solid curve) and sliding strain (dashed curve) are here seen not to be directly related. While the sliding strain increases monotonously with shortening, dilatation is observed to increase in a stepwise manner. During the first few centimeters of shortening the first thrust wedge is being activated and the model dilates more than 1%. Hereafter, a period of slight recompaction follows before the second back thrust is formed and dilatation increases 0.2%. Just after 10 cm of shortening the second thrust wedge initiates and dilatation jumps 0.7%. Again the model slightly recompacts after the thrust wedge is formed. After 15 cm of shortening the left wall starts to hinder further fault propagation, and the deformation style changes as material is forced to move up the left wall. Consequently, dilatation generally increases after 15 cm of shortening.

[48] The implicit handling of shearing related dilatation is one of the great advantages of using discrete methods for modeling granular flows. Although the exact dependence of dilatation rates on particle shapes and frictional properties is not yet well understood, the comparative ease with which complex dilatation effects can be simulated, favors discrete methods for modeling fault systems encountered in structural geology. Other advantages of the discrete particle-based methods relate to how the discrete methods readily handles complex geometries and extreme deformations.

[49] With existing discrete particle methods such as the traditional DEM algorithm of *Cundall and Strack* [1979], particle trajectories are calculated from assumptions of microphysical contact dynamics. However, although the methods have been improved for their use in macroscopic structural modeling [see, e.g., *Seyferth and Henk*, 2006], an appropriate macrophysical response can only be achieved by procedures designed to calibrate the microphysical parameters. In this paper and the companion paper [*Egholm*, 2007] we have demonstrated that the SDEM algorithm overcomes this ad hoc procedure by mapping macrophysical properties at the scale of the particle through explicit incorporation of the stress tensor. In so doing, we are able (1) to obviate the need for the ad hoc calibration of the macrophysical and microphysical response and (2) to reproduce fault and shear zone geometries observed in nature and analogue models in a much more faithful fashion than in other numerical methods appropriate to large strain analysis in cohesive, frictional material.

[50] For many discrete modeling applications the DEM parametric calibration procedure generally detracts from the models' utility. Typically, when modeling geologic processes computationally, the response of a simplified model is calculated and compared to observations made of the real system being modeled. If the observations and model response are consistent, the model is generally thought of as being a good model of the real system. In this case, the main benefit of the modeling process is in the fact that the model response, and the model processes leading to this response are well understood. The model is so simple that we understand its behavior fully, and in this way, light can be shed on the real processes causing the phenomena we see in nature.

[51] However, this important advantage of modeling can be lost if the modeler does not control the model input completely, and the DEM calibration procedure stands in the way of such full control. This is so, since no clear correlation exists between the methods microphysical parameterization and its macroscopic behavior. It is generally the latter we use for comparisons with observations, and

hence the link between model setup and model response is not fully understood.

[52] SDEM on the other hand is formulated to overcome this problem. Here the particle interaction is calculated from macroscopic constitutive rules, and the macroscopic behavior of a particle assemblage can readily be analyzed and explained on this basis. In result, the SDEM model response is more easily understood, as long as the macroscopic constitutive rule is accepted as the underlying model assumption.

[53] Given that SDEM offers new advances in modeling large deformation problems, including localization in narrow shear zones and problems requiring an exact parameterization of, e.g., friction related properties, it is of immediate interest to apply the SDEM modeling strategy in problems where lithological related strength contrasts are suspected to play an essential role. While the kinematics of, e.g., fault smears, listric faults and trishear systems are relatively well understood and documented by conceptual kinematic models, the dynamic conditions leading to these structures' formation are much more obscure. SDEM models can help bridge this unfortunate gap between kinematic and dynamic interpretations.

[54] **Acknowledgments.** This work was funded by the Carlsberg Foundation, Copenhagen. Reviews by Susanne Buiter and an anonymous reviewer greatly improved the manuscript as did helpful comments by Steffen Abe. Bo Holm Jacobsen, John Korstgård, Louis Moresi, and David May are also thanked for contributing useful input.

References

Buiter, S. J. H., A. Y. Babeyko, S. Ellis, T. A. Gerya, B. J. P. Kaus, A. Kellner, G. Schreurs, and Y. Yamada (2006), The numerical sandbox: comparison of model results for a shortening and an extension experiment, in *Analogue and Numerical Modelling of Crustal-Scale Processes*, edited by S. J. H. Buiter and G. Schreurs, *Geol. Soc. Spec. Publ.*, *253*, 29–64.

Burbridge, D. R., and J. Braun (2002), Numerical models of the evolution of accretionary wedges using the distinct-element method, *Geophys. J. Int.*, *148*, 542–561.

Colletta, B., J. Letouzey, R. Pinedo, J. Ballard, and P. Balé (1991), Computerized X-ray tomography analysis of sandbox models: Examples of thin-skinned thrust systems, *Geology*, *19*, 1063–1067.

Crook, A. J. L., D. R. J. Owen, S. M. Willson, and J. G. Yu (2006a), Benchmarks for the evolution of shear localisation with large relative sliding in frictional materials, *Comput. Methods Appl. Mech. Eng.*, *195*, 4991–5010.

Crook, A. J. L., S. M. Willson, J. G. Yu, and D. R. J. Owen (2006b), Predictive modelling of structure evolution in sandbox experiments, *J. Struct. Geol.*, *28*, 729–744.

Cundall, P., and O. Strack (1979), A discrete numerical model for granular assemblies, *Geotechnique*, *29*, 47–65.

Dahl, N. (1987), Eksperimentelle ekstensjonsbrudd i sand som følge av verticale basementbevegelser, Master's thesis, Dep. of Earth Sci., Univ. of Aarhus, Aarhus, Denmark.

Davis, D., J. Suppe, and F. A. Dahlen (1983), Mechanics of fold-and-thrust belts and accretionary wedges, *J. Geophys. Res.*, *88*, 1153–1172.

Donze, F., P. Mora, and S.-A. Magnier (1994), Numerical simulation of faults and shear zones, *Geophys. J. Int.*, *116*, 46–52.

Egholm, D. L. (2007), A new strategy for discrete element numerical models: 1. Theory, *J. Geophys. Res.*, doi:10.1029/2006JB004557, in press.

Ellis, S., G. Schreurs, and M. Panien (2004), Comparisons between analogue and numerical models of thrust wedge development, *J. Struct. Geol.*, *26*, 1659–1675.

Finch, E., S. Hardy, and R. Gawthorpe (2003), Discrete element modelling of contractional fault-propagation folding above rigid basement fault blocks, *J. Struct. Geol.*, *25*, 515–528.

Finch, E., S. Hardy, and R. Gawthorpe (2004), Discrete-element modelling of extensional fault-propagation folding above rigid basement fault blocks, *Basin Res.*, *16*, 489–506.

Fullsack, P. (1995), An arbitrary lagrangian-eulerian formulation for creeping flows and its application in tectonic models, *Geophys. J. Int.*, *120*, 1–23.

Gerya, T. V., and D. A. Yuen (2003), Characteristics-based marker-in-cell method with conservative finite-differences schemes for modeling geological flows with strongly variable transport properties, *Phys. Earth Planet. Inter.*, *140*, 293–318.

Itasca Consulting Group, Inc. (1999), PFC^{2D}, User Guide, version 3.0, Minneapolis, Minn.

Moresi, L., F. Dufour, and H. B. Mühlhaus (2002), Mantle convection modeling with viscoelastic/brittle lithosphere: Numerical methodology and plate tectonic modeling, *Pure Appl. Geophys.*, *159*, 2335–2356.

Patton, T., and R. Fletcher (1995), Mathematical block-motion model for deformation of a layer above a buried fault of arbitrary dip and sence of slip, *J. Struct. Geol.*, *17*, 1455–1472.

Schreurs, G., et al. (2006), Analogue benchmarks of shortening and extension experiments, in *Analogue and Numerical Modelling of Crustal-Scale Processes*, edited by S. J. H. Buiter and G. Schreurs, *Geol. Soc. Spec. Publ.*, *253*, 1–27.

Seyferth, M., and A. Henk (2006), A numerical sandbox: High-resolution distinct element models of halfgraben formation, *Int. J. Earth Sci.*, *95*, 189–203.

Storti, F., and K. McClay (1995), Influence of syntectonic sedimentation on thrust wedges in analogue models, *Geology*, *23*, 999–1002.

Strayer, L. M., P. J. Hudleston, and L. J. Lorig (2001), A numerical model of deformation and fluid-flow in an evolving thrust wedge, *Tectonophysics*, *335*, 121–145.

Vásárhelyi, B. (1999), Shear failure in rock using different constant normal load, *Period. Polytech. Civ. Eng.*, *43*(2), 179–186.

Vermeer, P. A. (1990), The orientation of shear bands in bi-axial tests, *Geotechnique*, *40*, 223–236.

Vermeer, P. A., and R. De Borst (1984), Non-associated plasticity for soils, concrete and rock, *Heron*, *29*, 1–62.

Withjack, M., J. Olson, and E. Peterson (1990), Experimental models of extensional forced folds, *AAPG Bull.*, *74*, 1038–1045.

O. R. Clausen, D. L. Egholm, and S. B. Nielsen, Department of Earth Sciences, University of Aarhus, Høegh-Guldbergs Gade 2, DK-8000 Aarhus C., Denmark. (david@geo.au.dk)

M. Sandiford, School of Earth Sciences, Melbourne University, Parkville, Vic 3010, Australia.